

Variational quantum simulation of valence-bond solids

Daniel Huerga^{1, 2, *}

¹*Stewart Blusson Quantum Matter Institute, University of British Columbia, V6T 1Z4 Vancouver, BC, Canada*

²*Department of Physical Chemistry, University of the Basque Country UPV/EHU, Apartado 644, 48080 Bilbao, Spain*

(Dated: January 10, 2022)

We introduce a hybrid quantum-classical variational algorithm to simulate ground-state phase diagrams of frustrated quantum spin models in the thermodynamic limit. The method is based on a cluster-Gutzwiller ansatz where the wave function of the cluster is provided by a parameterized quantum circuit. The key ingredient is a tunable real XY gate allowing to generate valence-bonds on nearest-neighbor qubits. Additional tunable single-qubit Z- and two-qubit ZZ-rotation gates permit the description of magnetically ordered phases while efficiently restricting the variational optimization to the U(1) symmetric subspace. We benchmark the method against the paradigmatic J_1 - J_2 Heisenberg model on the square lattice, for which the present hybrid ansatz is an exact realization of the cluster-Gutzwiller with 4-qubit clusters. In particular, we describe the Néel order and its continuous quantum phase transition onto a valence-bond solid characterized by a periodic pattern of 2×2 strongly-correlated plaquettes, providing a route to synthetically realize valence-bond solids with currently developed superconducting circuit devices.

I. INTRODUCTION

Hybrid quantum-classical variational algorithms, so-called variational quantum algorithms (VQA), are at the center of current research for their potentialities in providing first demonstrations of useful quantum computing applications with noisy intermediate scale quantum (NISQ) devices [1]. They consist in a feedback loop where the NISQ device provides a quantum state via a parameterized quantum circuit (PQC) that is tuned by a classical computer so as to optimize an objective function encoding the target problem [2–4]. The variational quantum eigensolver was the first hybrid algorithm proposed to approximate the ground-state and energy of *finite* strongly-correlated fermionic Hamiltonians as an alternative to the phase estimation algorithm [5], which provides the exact ground-state solution but requires coherence times unreachable with current NISQ technology [6].

The initially expected unleashed potentialities of VQA towards providing quantum advantage on problems including machine learning, optimization, and the simulation of strongly-correlated electron systems —a foundational motivation driving research in quantum computation [7–12]— have been narrowed down due to the identification of various limitations. Specifically, the optimization landscape has been shown to be plagued with so-called *barren plateaux* [13], which may appear independently of the optimization routine used [14], and sub-optimal minima, which has been argued to render the classical optimization problem NP-hard [15]. In spite of these limitations, *local* objective functions, e.g. the energy of a local Hamiltonian, may still be efficiently optimized for shallow PQCs in certain regimes [16].

Here, we introduce a VQA to simulate ground-state

phase diagrams of frustrated two-dimensional (2D) quantum spin models in the thermodynamic limit considering currently developed superconducting qubit chips with squared connectivity [17, 18]. Frustrated quantum magnets are characterized by the impossibility of finding a spin arrangement satisfying all local energy constraints simultaneously in any locally-rotated basis [19]. They pose a challenge to state-of-the-art classical numerical methods [20–22] and at the same time host a plethora of phases and phenomena of both fundamental and applied interest. In particular, quantum paramagnetic phases, which may either break or preserve translational symmetry —so-called valence-bond solids (VBS) and quantum spin-liquids (QSL), respectively— have important implications for material science [23–25] and quantum computation [26–31].

The method here introduced is built upon the grounds of hierarchical mean-field theory (HMFT), an algebraic framework based on the identification of clusters as the building blocks containing the essential symmetries and correlations to describe a system [32]. A cluster-Gutzwiller ansatz represents the lowest order approximation which, harnessed with a scaling analysis, allows to unveil quantum phases and phase transitions characterized by competition or coexistence of different orders, including VBS states [33–39]. More specifically, we present a *quantum-assisted* approach to HMFT (Q-HMFT) where the cluster wave function is provided by a U(1) symmetry-preserving PQC. Its central building block is a two-qubit XY gate allowing to generate valence-bonds on nearest-neighbor qubits, while efficiently restricting the variational search to the null magnetization sector of a SU(2) target Hamiltonian. Information about the thermodynamic limit including the explicit description of symmetry breakdown and onset of long-range orders is implemented at the objective function level (i.e. the energy) through a self-consistent mean-field embedding concomitant to the cluster-Gutzwiller approach.

* daniel.huerga@ubc.ca

To the best of our knowledge, this is the first VQA proposal to simulate 2D frustrated quantum magnets in the thermodynamic limit with superconducting qubit technology. Recently, a symmetry-preserving PQC constructions have been utilized to quantum simulate 1D finite frustrated quantum magnets with trapped-ions [40], as well as purification protocols have been proposed to simulate infinite 2D fermionic systems with analog quantum simulators [41]. Other cluster-embedding hybrid proposals to approach the thermodynamic limit have been centered on the simulation of fermionic Hamiltonians [42–44]. On the other hand, hybrid quantum-classical tensor network approaches permit the simulation of frustrated quantum magnets on infinite chains [45–47], and have been proposed to simulate 2D finite systems with fewer qubits than the target Hamiltonian [48].

We benchmark Q-HMFT on the antiferromagnetic J_1 - J_2 model on the square lattice, a paradigmatic model of frustrated quantum magnetism hosting Néel, quantum paramagnetic and columnar antiferromagnetic (CAF) phases. In particular, the ultimate nature of the quantum paramagnetic phase and its driving mechanisms is still a matter of debate. Proposals have fluctuated through the time, including the stabilization of a VBS phase characterized by the periodic patterns of either four-spin *plaquettes* preserving the C_4 symmetry of the lattice [49–51] or two-spin *dimers* breaking it [52, 53], or the emergence of different types of QSLs [54–59]. We simulate noiseless realizations of Q-HMFT with $L \times L$ clusters of $N=4$ and $N=16$ qubits ($L=2$ and $L=4$, respectively) and find a very good quantitative approximation to previous HMFT calculations with the same cluster sizes [35]. Specifically, with 4-qubit clusters, Q-HMFT results in an *exact* hybrid realization of the cluster-Gutzwiller wave function allowing to describe ordered Néel and CAF phases, as well as a *plaquette*-VBS. With 16-qubit clusters, Q-HMFT results in a good quantitative approximation to its classical counterpart, which essentially provides a renormalization of the phase diagram obtained with 4-qubits. Although the shallow PQC construction results in a plaquette-VBS slightly favoring one direction of the plane and thus breaking C_4 symmetry, our numerical results support that such a symmetry is smoothly recovered upon increasing the number of layers of the PQC.

The definition of the energy (i.e. the objective function) in the thermodynamic or infinite lattice limit explicitly provides a means to inspect quantum phase transitions. Specifically, it allows to identify a continuous vanishing of the Néel order into the plaquette-VBS and the subsequent first order transition to the CAF. The use of XY gates makes the circuit depth shallower with respect to other ansatze that either admix symmetry sectors [60, 61] or that may require higher chip connectivities [11]. In spite of its shorter depth, the variance of the gradient shows an exponential decrease upon increasing the cluster size, hinting to the presence of barren plateaux impeding an efficient scaling to clusters of larger size, $L > 4$. Nevertheless, Q-HMFT provides a first proposal

towards the hybrid simulation of plaquette-VBS states and their continuous transition onto ordered states with superconducting qubit technology.

The outline of the paper is as follows. In Sec. II we describe in detail the Q-HMFT algorithm and the symmetry-guided PQC construction. In Sec. III we provide with benchmark results on the J_1 - J_2 model on the square lattice. Specifically, we compute ground-state energy and its first derivative to uncover the phase diagram, as well as magnetization and dimer observables to characterize the phases with 2×2 and 4×4 clusters, and compare with HMFT results. Additionally, we compute the variance of the gradient upon increasing the cluster size. In Sec. IV, we close with a summary and an outlook discussing possible extensions of the present study.

II. QUANTUM-ASSISTED HIERARCHICAL MEAN-FIELD

Let us consider a generic translational invariant 2-body local Hamiltonian in the infinite lattice, $H = \sum_{i,j} h_{i,j}$, where $h_{i,j} = J_{i,j} \mathbf{S}_i \mathbf{S}_j$ and $\mathbf{S}_i = (S_i^x, S_i^y, S_i^z)$ refers to the $S=1/2$ SU(2) spin operators at site i , and $J_{i,j}$ to the two-spin interaction strength. We tile the lattice with N -site equivalent clusters preserving as much as possible the original symmetries of the lattice. We classify the Hamiltonian terms on those acting within clusters, $h_R^\square = \sum_{(i,j) \in R} h_{i,j}$, and those acting on two different clusters, $h_{R,R'}^I = \sum_{i \in R, j \in R'} h_{i,j}$, where R labels the position of the cluster in the tiled lattice, or superlattice. We define a uniform cluster-Gutzwiller ansatz as the product state of N -site clusters, all in the same state parameterized by $\boldsymbol{\theta} = \{\theta_k\}$,

$$|\Psi\rangle = \bigotimes_R |\psi_{\boldsymbol{\theta}}\rangle. \quad (1)$$

When $\boldsymbol{\theta} = \{\theta_k\}$ uncovers the whole cluster Hilbert space, this ansatz provides an unbiased approximation as long as the characteristic length of competing phases lie within its size. Considering wave function (1), the energy density of a generic two-body local Hamiltonian is

$$E_{\boldsymbol{\theta}} = \frac{1}{N} \left(\langle h^\square \rangle_{\boldsymbol{\theta}} + \frac{1}{2} \sum_{i \in \square, j \in \square'} J_{i,j} \langle \mathbf{S}_i \rangle_{\boldsymbol{\theta}} \langle \mathbf{S}_j \rangle_{\boldsymbol{\theta}} \right), \quad (2)$$

where $\langle \cdot \rangle_{\boldsymbol{\theta}}$ refers to the expectation value with the parameterized cluster wave function (1) and we have drop the cluster index. The first summand in (2) accounts for the intra-cluster energy contribution of cluster \square , while the second runs over all two-spin inter-cluster interactions with neighboring clusters, \square' , the $1/2$ preventing double counting. This second term provides information about the thermodynamic limit by allowing the breakdown of symmetries and concomitant onset of long-range order. Generalization to n -body interactions appearing

in e.g. ring-exchange models is straightforward, although tedious [33, 37, 39].

The set of optimal energy and parameters, $E = E_{\theta^*}$ and θ^* , respectively, is obtained upon minimization of the variational energy (2) by Rayleigh-Ritz variational principle and thus provides with an upper bound to the exact energy in the thermodynamic limit. Upon coarse graining the cluster, the method allows to assess the stability of the phases and phase transitions found with the a smaller cluster size [34–36, 38]. However, with classical computing resources cluster sizes are limited at $N \lesssim 30$ due to the exponential increase of the Hilbert space, which conforms the major bottleneck of this approximation towards unveiling the ultimate nature of phases with closely competing paramagnetic orders.

In order to further extend the scaling analysis, we may consider the cluster wave function generated by a PQC,

$$|\psi_{\theta}\rangle = \prod_{k=1}^m U_k(\theta_k) |\psi_0\rangle, \quad (3)$$

where $|\psi_0\rangle$ is an initial easy-to-prepare state, here onwards fixed to $|\psi_0\rangle = |0101\dots01\rangle$ for reasons that will be clear below, with $|0\rangle \doteq |\uparrow\rangle$, $|1\rangle \doteq |\downarrow\rangle$, and $U_k(\theta_k) = e^{-i\theta_k V_k}$, where V_k is an hermitian operator acting on either one or two qubits.

For Hamiltonians possesing SU(2) symmetry on a bipartite lattice, we may restrict the variational search to the U(1) symmetry preserving subspace of null total magnetization, $\sum_j S_j^z = 0$. The most general continuously parameterized gate in the two-qubit null-magnetization space is generated by the Heisenberg and z -projection of Dzyaloshinskii-Moriya (DM) interactions, i.e. $V_{ij} = J(S_i^x S_j^x + S_i^y S_j^y) + D(\mathbf{S}_i \times \mathbf{S}_j)^z$,

$$U_{ij}(\theta, \beta) = e^{-i\theta(e^{-i\beta} S_i^+ S_j^- + e^{i\beta} S_j^+ S_i^-)}, \quad (4)$$

where $S_i^{\pm} = (S_i^x \pm iS_i^y)$ are the SU(2) ladder operators, $\beta = \arctan(D/J)$, and we have reabsorbed $\sqrt{J^2 + D^2}$ in θ without loss of generality. Considering that the most general variational cluster wave function of the form (1) is purely real within this subspace, the simplest gate inducing local VBS order is the *real* XY gate,

$$U_{ij}^{\text{XY}}(\theta) = \begin{pmatrix} 1 & 0 & 0 & 0 \\ 0 & \cos(\theta) & \sin(\theta) & 0 \\ 0 & -\sin(\theta) & \cos(\theta) & 0 \\ 0 & 0 & 0 & 1 \end{pmatrix}, \quad (5)$$

which is purely generated by the DM interactions, i.e. $U_{ij}^{\text{XY}}(\theta) = U_{ij}(\theta, \pi/2)$.

The computational power of the family of XY Heisenberg gates ($\beta=0$) has been extensively studied [62–65] and demonstrated its universality [66]. From the experimental standpoint, recent implementations of the most general XY gate of Eq. (4) have shown fidelities of the order $\sim 97\%$ [67]. Closely related two-qubit tunable Heisenberg interaction [68] as well as iSWAP-like gates

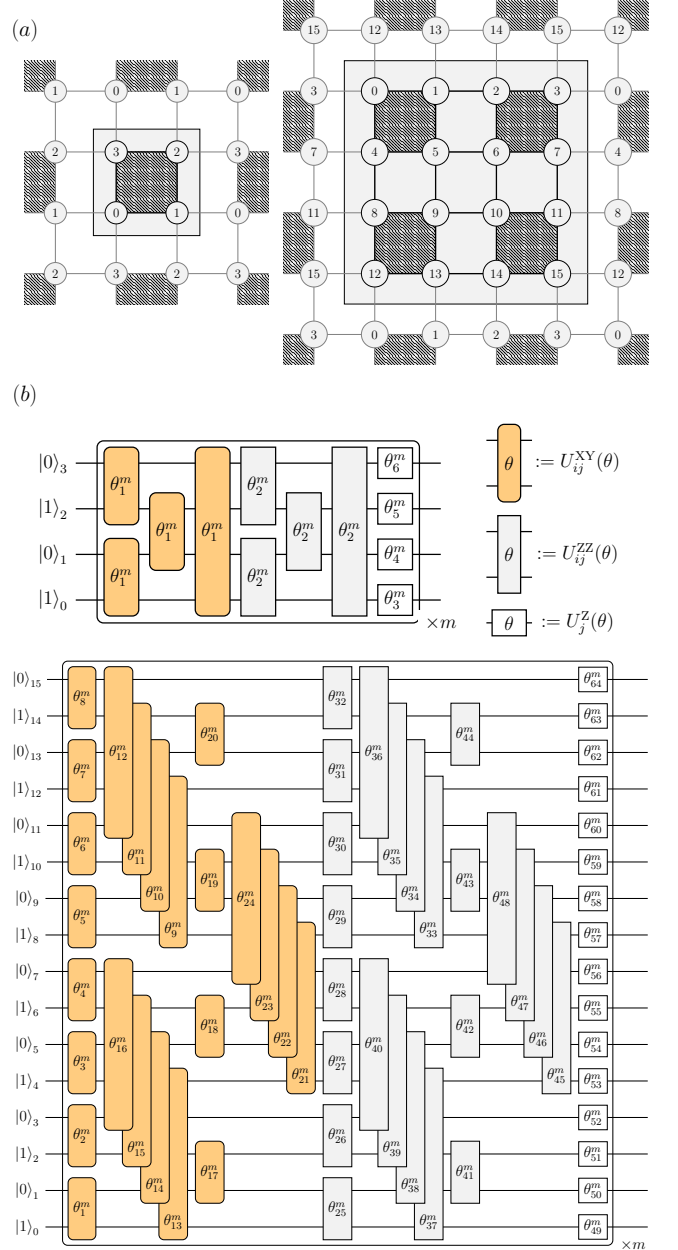


FIG. 1. (a) Labeling of the cluster and its near embedding environment after having tiled the lattice with equivalent 2×2 (left) and 4×4 (right) clusters. Hatched shadows represent the plaquette-VBS ordering. (b) Parameterized quantum circuit (PQC) providing the cluster wave function (3). Qubits follow the labeling in (a) and XY- and ZZ-rotation are represented by orange-rounded and gray rectangular blocks, respectively, while white squares represent single-qubit Z-rotation gates. The whole set of layers is repeated m times.

[69, 70] are realizable with even higher fidelities. Here, the use of the *real*-XY gate (5) stems from the observation that it transforms a trivial (i.e. uncorrelated) Néel

state into a two-spin singlet, i.e. a valence-bond,

$$U_{ij}^{XY} \left(\frac{\pi}{4} \right) |01\rangle_{ij} = \frac{1}{\sqrt{2}} \left(|01\rangle_{ij} - |10\rangle_{ij} \right). \quad (6)$$

We consider currently developed squared connectivities [17, 18] and $L \times L$ clusters with $L=2$ and $L=4$ and construct the PQC by applying the two-qubit XY gates (5) to nearest-neighbor bonds in an order that favors the C_4 symmetry of the square lattice and minimizes the total number of layers of the circuit, ℓ , as it is schematically shown in Fig. (1). We increase the amount of correlations by adding a set of complex two-qubit tunable ZZ-rotation gates to nearest-neighbor qubits, $U_{ij}^{ZZ}(\theta) = e^{-i\theta Z_i Z_j}$, where $Z_i = 2S_i^z$. We add a final layer of single-qubit arbitrary-angle Z-rotation gates, $U_j^Z(\theta) = e^{-i\theta Z_j}$, to compensate for the non-trivial phases introduced by the ZZ-rotation gates. Both of these gates can be efficiently realized experimentally [71]. Such a *macro-layer* is repeated m times. For the 2×2 cluster, each macro-layer has $\ell=5$ layers, while for $L \geq 4$, it has a fixed number of $\ell=9$ layers.

III. NUMERICAL RESULTS

We benchmark Q-HMFT against the antiferromagnetic J_1-J_2 Heisenberg model on the square lattice, a paradigmatic model of frustrated quantum magnetism in 2D originally motivated by the physics of cuprate superconductors,

$$H = J_1 \sum_{\langle i,j \rangle} \mathbf{S}_i \mathbf{S}_j + J_2 \sum_{\langle\langle i,j \rangle\rangle} \mathbf{S}_i \mathbf{S}_j, \quad (7)$$

where $\langle i,j \rangle$ and $\langle\langle i,j \rangle\rangle$ account for nearest-neighbor and next-to-nearest neighbors pairs of sites, respectively. From here onwards, we express all quantities in units of J_1 . Upon tuning $J_2 > 0$, model (7) hosts a long-range ordered Néel phase, a quantum paramagnetic phase, and a columnar antiferromagnetic (CAF) phase. The ultimate nature of the VBS phase is a long-standing matter of debate [49–57], latest studies based on density-matrix renormalization group computations on $2L \times L$ clusters arguing in favor of the onset of either dimer [58] or plaquette orders [59] through an intermediate QSL phase. Classical HMFT computations with $N=4$ and $N=16$ clusters provide a picture consistent with Landau theory, where the Néel order melts through a second order transition into a C_4 symmetric plaquette-VBS characterized by 4-spin strongly resonating plaquettes through a second order transition, before entering the CAF through a first order transition [35]. Interestingly, upon introducing a third nearest neighbor Heisenberg interaction, the plaquette-VBS order has been argued to become stronger [50] and, more recently, to be a higher-order symmetry-protected topological phase [72].

Specifically, we perform *ideal* classical simulations of Q-HMFT on the J_1-J_2 model (7), i.e. considering noiseless gates and as if we carried out infinite number of

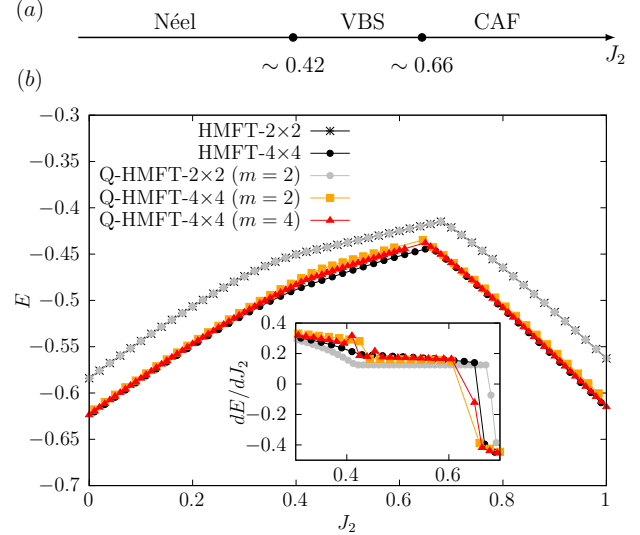


FIG. 2. (a) Schematic phase diagram of the J_1-J_2 model (7) as computed with Q-HMFT. (b) Energy per spin computed with Q-HMFT- 2×2 and $m=2$ (gray circles), and Q-HMFT- 4×4 and $m=2$ (orange squares) and $m=4$ (red triangles), together with HMFT results for comparison. Q-HMFT- 2×2 reproduces exactly HMFT results with the same cluster.

independent measurements (so-called shots). As a classical optimizer, we use the gradient-based L-BFGS-B algorithm [73, 74], where the gradient of the energy is computed via two-point first order approximation, $\partial_{\theta_k} E = (E_{\theta+\delta} - E_{\theta})/|\delta|$, for $\delta = 10^{-10}$ along k direction in variational space. We compute the energy (2) and its derivatives, as well as order parameters, i.e. magnetization and dimer order with $N=4$ (2×2) and $N=16$ (4×4) clusters with $m=2$ and $m=4$ macro-layers, shown in Fig. (1). At points $J_2=0.0$, 0.5 , and 1.0 (each one deep in the phase) we take 1 optimal solution out of 10 optimizations starting at different parameter seeds, what generates three different optimal seeds for each of the three phases. As it is shown in the following, Q-HMFT- 2×2 with just $m=2$ macro-layers reproduces the HMFT results with the same cluster, providing an *exact* quantum circuit realization of the HMFT approach on this model, and thus of a plaquette-VBS.

In Fig. 2, we show the optimal energy per spin with respect to J_2 as computed with Q-HMFT with 2×2 clusters and $m=2$ macro-layers, and 4×4 cluster and $m=2$ and $m=4$ macro-layers, together with HMFT results with the same cluster sizes for comparison. In all approaches, upon inspecting the energy derivatives, we can distinguish two phase transitions. Specifically, Q-HMFT- 2×2 with $m=2$ exactly reproduces the HMFT energy results with the same cluster size. Upon inspecting the first derivative, we distinguish a continuous (second order) transition at $J_2 \simeq 0.42$ and a first order transition at $J_2 \simeq 0.68$. When increasing the cluster size to 4×4 , Q-HMFT improves the variational energy and approaches tightly HMFT- 4×4 as we increase the number of macro-

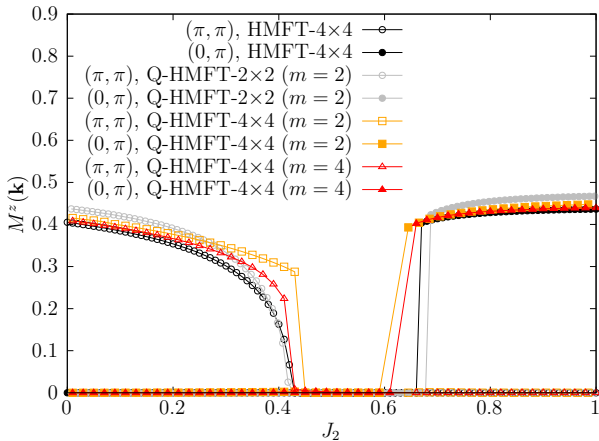


FIG. 3. Néel (empty points) and CAF (full points) order parameters computed with Q-HMFT- 2×2 with $m=2$ macro-layers (gray circles), Q-HMFT- 4×4 with $m=2$ (orange squares) and $m=4$ (red triangles), together with HMFT- 4×4 results (black circles) for comparison.

layers from $m=2$ to $m=4$. In particular, the most significant energy difference, corresponding to the intermediate phase, reduces considerably. Concerning the order of phase transitions, Q-HMFT- 4×4 shows a weak first order transition with at $J_2 \simeq 0.44$ for $m=2$, which smoothes and moves towards the second order phase transition found at $J_2 \simeq 0.42$ with HMFT- 4×4 in Ref. [35] upon increasing the number of macro-layers to $m=4$ (see inset). At $J_2 \simeq 0.64$ it is found a first order transition with $m=2$ that moves towards $J_2 \simeq 0.65$ upon increasing to $m=4$, approaching the HMFT- 4×4 result ($J_2 \simeq 0.66$). In both transitions, we find some numerical instabilities within Q-HMFT. We will further investigate such differences upon inspecting the magnetization and dimer observables in the following.

First, to characterize the phases, we inspect the magnetization depending on the reciprocal vector,

$$M^z(\mathbf{k}) = \frac{1}{N} \sum_j e^{-i\mathbf{r}_j \cdot \mathbf{k}} \langle S_j^z \rangle, \quad (8)$$

where $\mathbf{r}_i = (r_i^x, r_i^y)$ refers to the position of site i in the infinite lattice and \mathbf{k} to a vector in the first Brillouin zone, which provides the order parameters characterizing Néel and CAF orders, at $\mathbf{k} = (\pi, \pi)$ and $\mathbf{k} = (0, \pi)$ (equivalently, $\mathbf{k} = (\pi, 0)$), respectively. In Fig. (3) we show Q-HMFT results on the magnetization together with HMFT- 4×4 for comparison. As expected, Q-HMFT- 2×2 with $m=2$ reproduces exactly HMFT results with the same cluster (not shown for clarity purposes), showing the continuous vanishing of the Néel order parameter, characteristic of a second order transition, and the discontinuous onset of CAF order, characteristic of first order transitions. The magnetization is null in the intermediate phase, i.e. $\langle \mathbf{S}_j \rangle = 0$ for all j . With 4×4 clusters, Q-HMFT describes a slightly stronger Néel ordering than

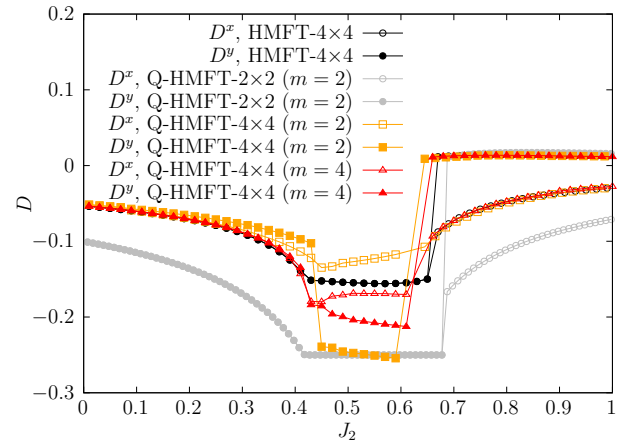


FIG. 4. Dimer observable (9) along the x (empty points) and y (full points) directions as computed with the Q-HMFT ansatz with 2×2 , $m=2$ (gray circles) and 4×4 clusters and $m=2$ (orange squares) and $m=4$ (red triangles), together with HMFT- 4×4 results (black circles) provided for comparison. An almost constant value of equal $D^x = D^y$ within the quantum paramagnetic phase $0.42 \lesssim J_2 \lesssim 0.66$ indicates the onset of a C_4 symmetric plaquette-VBS order within HMFT. Q-HMFT- 4×4 shows a preferred dimerization direction within this intermediate paramagnetic phase that is reduced upon increasing the number of macro-layers to $m=4$.

its classical counterpart, HMFT- 4×4 . Such a difference increases as we tune the J_2 interaction and the system approaches the quantum phase transition to the paramagnetic intermediate phase, resulting in a discontinuous vanishing of the Néel order parameter, consistent with the first order transition observed through computation of the energy. Upon increasing the macro-layers to $m=4$, such a jump reduces, indicating that the first order transition closes into a second order transition for $m > 4$, approaching the HMFT- 4×4 result. On the other hand, the CAF order is quantitatively well approximated with $m=2$.

Second, in order to describe the nature of the intermediate paramagnetic phase, we define a dimer observable providing information on the onset of dimerization along $\alpha = x, y$ directions,

$$D^\alpha = \frac{1}{L} \sum_{\langle i,j \rangle_\alpha} (-1)^{r_i^\alpha} \langle \mathbf{S}_i \mathbf{S}_j \rangle, \quad (9)$$

where $\langle i, j \rangle_\alpha$ refers to nearest-neighbor bonds along α . Technically, considering the periodicity of the cluster-Gutzwiller wave function, the sum in Eq. (9) reduces to all intra- and outer-cluster bonds of a single cluster in each of the directions. Notice that (9) is not an order parameter in the strict sense (i.e. non-zero within the VBS phase, and null otherwise), but an observable defined as a means to signal out the emergence of dimerization and breakdown of translational invariance and C_4 symmetry, both discrete symmetries. Specifically, $D^x \neq D^y$ signals dimerization in a preferred direction, while $D^x = D^y$ pro-

vide a signature of a C_4 preserving state and eventual onset of plaquette order.

In Fig. (4) we show the dimer observable (9) along $\alpha = x, y$ directions as computed with Q-HMFT, providing HMFT results as a reference. For 2×2 clusters, same as with the magnetization, the Q-HMFT reproduces exactly HMFT results (not shown for clarity purposes), showing a non-zero $D^x = D^y$ within the Néel phase that increases in absolute value and reaches a constant value at precisely the second order transition point found when inspecting the energy (Fig. (2)) and magnetization (Fig. (3)), indicating the onset of a C_4 symmetric plaquette-VBS. Upon further tuning J_2 , the dimer observables shows a discontinuity corresponding to the first order phase transition to the CAF phase, and shows $D^y > D^x$ consistent with the onset of antiferromagnetic order in the y -direction. Upon increasing the cluster size to 4×4 , HMFT shows essentially the same trend, although the absolute value of the dimer observable in both directions is reduced approximately by a factor of 2 throughout the whole phase diagram. Q-HMFT- 4×4 with $m=2$ macro-layers approximate quantitatively well the dimer observable as computed with HMFT within the Néel and CAF. Within the paramagnetic intermediate region, the dimer observable shows a slight stronger dimerization in one of the directions, breaking the C_4 symmetry of the plaquette-VBS, when computed with Q-HMFT. Such a difference is reduced upon increasing the number of macro-layers to $m=4$, indicating that the full C_4 symmetric plaquette-VBS might be recovered upon increasing the number of macro-layers.

Notice that with the cluster-Gutzwiller ansatz (1), paramagnetic phases are described as a product of N -qubit singlet states (i.e. all self-consistent mean-fields are zero, irrespective of the initial point in the variational optimization). The dimer observable shown in Fig. (4) indicates that the cluster-Gutzwiller wave function (both within Q- and classical HMFT) contains a pattern of correlated 2×2 plaquettes, also found with other numerical techniques [49–51, 58]. Specifically, within the Q-HMFT- 2×2 , the plaquette-VBS is described by an uncorrelated product of C_4 symmetric 4-qubit states,

$$|\psi_{\square}\rangle = -\alpha (|0101\rangle + |1010\rangle) + \beta (|1100\rangle + |0110\rangle + |0011\rangle + |1001\rangle), \quad (10)$$

where $\alpha, \beta > 0$ and states are referred in the computational basis $|\{n_j\}\rangle$ at positions j described in Fig. (1). At $J_2=0.5$, $\alpha \simeq 0.577$ and $\beta \simeq 0.289$. Further correlations among the 2×2 plaquettes are included when increasing the cluster size (Q- and HMFT- 4×4), but the same plaquette ordering prevails.

Last, we study the potential scaling of the algorithm towards using clusters $L > 4$ and the eventual emergence of the infamous barren-plateaux in the optimization landscape upon increasing the size of the cluster [13, 16]. We compute the first derivative with respect to the first variational parameter (θ_1^1) of the PQC with $N=4$ and $N=16$ clusters with fixed $m=2$ (Fig. 1) by sampling 100 ran-

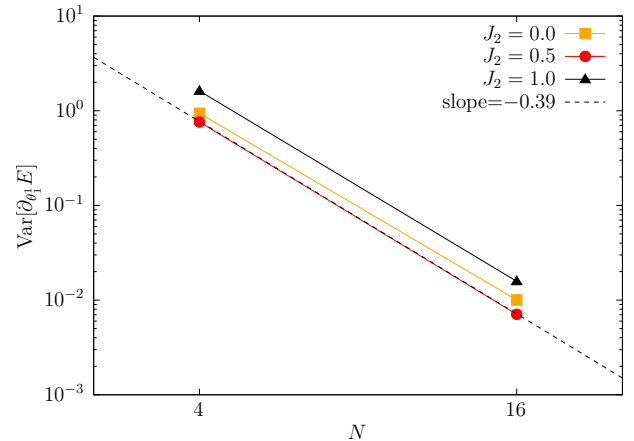


FIG. 5. Variance of the derivative of the energy with respect to the first variational parameter plotted with respect to the number of qubits of the cluster for fixed macro-layer $m=2$ at $J_2=0.0$ (orange squares), $J_2=0.5$ (red circles), and $J_2=1.0$ (black triangles). Lines are a guide to the eye. We observe an exponential vanishing indicating the emergence of barren plateaux with increasing cluster size.

dom points in the variational manifold. As seen in Fig. 5, the variance of the gradient is exponentially suppressed upon coarse-graining Q-HMFT from 2×2 to 4×4 clusters, indicating that barren-plateaux emerge, although with smaller exponent than what was found with other symmetry-breaking PQC [13].

IV. SUMMARY AND OUTLOOK

Models of frustrated quantum magnetism pose severe hurdles to state-of-the-art computational approaches, while at the same time host a plethora of exotic phases, some of which are relevant for the development of quantum computing devices. In particular, two-dimensional paramagnetic valence bond solids (VBS) are potential sources for quantum computation. Therefore, both from the fundamental as well as from the applied standpoints, these systems offer a natural testbed to develop new hybrid algorithms to be carried out in NISQ devices.

We have presented a hybrid algorithm to quantum simulate 2D quantum frustrated magnets in the thermodynamic limit, and in particular, VBS states. The method builds upon the grounds of hierarchical mean-field theory (HMFT), a state-of-the-art classical algorithm using clusters as its building block, for which the cluster-Gutzwiller ansatz represents the lowest order approximation. The quantum-assisted approach to HMFT here presented (dubbed Q-HMFT) makes use of a parameterized quantum circuit (PQC) to generate the wave function of the cluster considering currently developed superconducting chips with square connectivities. The main building block of such PQC is a two-qubit real XY gate allowing to easily generate valence-bonds, the main ingre-

dient of VBS phases. Together with additional layers of tunable two-qubit ZZ- and single-qubit Z-rotations, they furnish a U(1) preserving *macro-layer* that efficiently restricts the variational search and reduces circuit depths with respect to other commonly used PQC constructions that admix symmetry sectors [60, 61].

We have provided benchmark results of Q-HMFT on the J_1 - J_2 model on the square lattice, which had been previously studied by classical HMFT means [35]. The numerical simulations of the ideal Q-HMFT algorithm on ground-state energy, magnetization, and dimer observables by means of $N=4$ and $N=16$ $L \times L$ clusters show that the PQC above described allows to uncover Néel and columnar antiferromagnet (CAF) long-range ordered phases, as well as their meltdown into a *plaquette*-VBS. Remarkably, the 4-qubit Q-HMFT with just $m=2$ macro-layers provides an *exact* circuit realization of the cluster-Gutzwiller ansatz for this target Hamiltonian, allowing to describe a continuous second order phase transition of the Néel onto the *plaquette*-VBS. Although the Q-HMFT- 4×4 is not the exact realization of the cluster-Gutzwiller with the same cluster, it provides a quantitative good approximation and thus a compressed variational description of it. That is, the Q-HMFT- 4×4 ansatz has just $64m$ variational parameters while its classical counterpart has 12870, i.e. the dimension of the $S^z = 0$ sector. Nevertheless, upon studying the variance of the gradient we have shown that the use of XY gates does not prevent the emergence of barren plateaux upon scaling from $N=4$ to $N=16$.

In conclusion, the work here presented provides a route towards the quantum simulation of 2D frustrated quantum magnets in the thermodynamic limit and, in particular, VBS phases with currently developed 4- and 16-qubit superconducting chips. Interestingly, the *plaquette*-VBS here described has been recently argued to be characterized by a non-trivial symmetry-protected topological order that can be *locally* probed upon inserting a flux into a 2×2 plaquette of the lattice [75, 76]. The generic tunable XY gate provides a direct means for such flux

insertion into the wave function generated by the PQC.

Further investigation in ways to overcome the barren plateaux phenomenon should ultimately be carried out for an efficient scaling of the algorithm. They may include the exploration of alternative U(1) symmetric constructions of the PQC, including combination with hybrid realization of tensor network inspired ansätze to reduce the number of qubits [45–48], or the use of collective gates native to other technologies, which may inherently preserve the lattice rotational symmetries. In particular, trapped-ion systems can tune collective long-range XY gates on 2D lattices of different topologies [77], which in addition may allow to quantum simulate other interesting VBS states, such as the localized resonant magnon states of the kagome lattice [38, 78].

On the other hand, extensions of this work may include the implementation of error mitigation strategies based on symmetry [79], the description of low-energy excitations over the ground-state, for which HMFT has a well-established framework [35, 36], or the benchmark of optimization routines and quantum hardware on exactly solvable models possessing VBS as exact ground-states [39, 80]. From the experimental standpoint, we expect these results to motivate further development and refinement of the general tunable XY gates as key elements for variational quantum algorithms.

ACKNOWLEDGMENTS

We are pleased to acknowledge interesting discussions with A. Parra-Rodriguez, Christopher Eichler, Gerardo Ortiz, and Robert Raussendorf. We gratefully acknowledge G. Ortiz for providing access to computing facilities of the Department of Physics, Indiana University. We acknowledge financial support from OpenSuperQ project (grant agreement 820363) of the EU Quantum Flagship program. DH is funded by the Canada First Research Excellence Fund, Quantum Materials and Future Technologies Program.

[1] J. Preskill, *Quantum* **2**, 79 (2018).

[2] J. R. McClean, J. Romero, R. Babbush, and A. Aspuru-Guzik, *New Journal of Physics* **18**, 023023 (2016).

[3] M. Cerezo, A. Arrasmith, R. Babbush, S. C. Benjamin, S. Endo, K. Fujii, J. R. McClean, K. Mitarai, X. Yuan, L. Cincio, and et al., *Nature Reviews Physics* **3**, 625 (2021).

[4] K. Bharti, A. Cervera-Lierta, T. H. Kyaw, T. Haug, S. Alperin-Lea, A. Anand, M. Degroote, H. Heimonen, J. S. Kottmann, T. Menke, W.-K. Mok, S. Sim, L.-C. Kwek, and A. Aspuru-Guzik, (2021), arXiv:2101.08448 [quant-ph].

[5] A. Peruzzo, J. McClean, P. Shadbolt, M.-H. Yung, X.-Q. Zhou, P. J. Love, A. Aspuru-Guzik, and J. L. O’Brien, *Nature Communications* **5**, 4213 (2014).

[6] M. A. Nielsen and I. L. Chuang, *Quantum Computation and Quantum Information: 10th Anniversary Edition* (Cambridge University Press, 2010).

[7] R. P. Feynman, *International journal of theoretical physics* **21**, 467 (1982).

[8] D. S. Abrams and S. Lloyd, *Physical Review Letters* **79**, 2586 (1997).

[9] G. Ortiz, J. E. Gubernatis, E. Knill, and R. Laflamme, *Physical Review A* **64** (2001), 10.1103/physreva.64.022319.

[10] R. Somma, G. Ortiz, J. E. Gubernatis, E. Knill, and R. Laflamme, *Physical Review A* **65** (2002), 10.1103/physreva.65.042323.

[11] D. Wecker, M. B. Hastings, and M. Troyer, *Phys. Rev. A* **92**, 042303 (2015).

[12] Z. Jiang, K. J. Sung, K. Kechedzhi, V. N. Smelyanskiy, and S. Boixo, *Physical Review Applied* **9** (2018),

10.1103/physrevapplied.9.044036.

[13] J. R. McClean, S. Boixo, V. N. Smelyanskiy, R. Babbush, and H. Neven, *Nature Communications* **9**, 4812 (2018).

[14] A. Arrasmith, M. Cerezo, P. Czarnik, L. Cincio, and P. J. Coles, “Effect of barren plateaus on gradient-free optimization,” (2020), arXiv:2011.12245 [quant-ph].

[15] L. Bittel and M. Kliesch, *Phys. Rev. Lett.* **127**, 120502 (2021).

[16] M. Cerezo, A. Sone, T. Volkoff, L. Cincio, and P. J. Coles, *Nature Communications* **12** (2021), 10.1038/s41467-021-21728-w.

[17] F. Arute, K. Arya, R. Babbush, D. Bacon, J. C. Bardin, R. Barends, R. Biswas, S. Boixo, F. G. S. L. Brandao, D. A. Buell, B. Burkett, Y. Chen, Z. Chen, B. Chiaro, R. Collins, W. Courtney, A. Dunsworth, E. Farhi, B. Foxen, A. Fowler, C. Gidney, M. Giustina, R. Graff, K. Guerin, S. Habegger, M. P. Harrigan, M. J. Hartmann, A. Ho, M. Hoffmann, T. Huang, T. S. Humble, S. V. Isakov, E. Jeffrey, Z. Jiang, D. Kafri, K. Kechedzhi, J. Kelly, P. V. Klimov, S. Knysh, A. Korotkov, F. Kostritsa, D. Landhuis, M. Lindmark, E. Lucero, D. Lyakh, S. Mandrà, J. R. McClean, M. McEwen, A. Megrant, X. Mi, K. Michelsen, M. Mohseni, J. Mutus, O. Naaman, M. Neeley, C. Neill, M. Y. Niu, E. Ostby, A. Petukhov, J. C. Platt, C. Quintana, E. G. Rieffel, P. Roushan, N. C. Rubin, D. Sank, K. J. Satzinger, V. Smelyanskiy, K. J. Sung, M. D. Trevithick, A. Vainsencher, B. Villalonga, T. White, Z. J. Yao, P. Yeh, A. Zaleman, H. Neven, and J. M. Martinis, *Nature* **574**, 505 (2019).

[18] S. Krinner, N. Lacroix, A. Remm, A. D. Paolo, E. Genois, C. Leroux, C. Hellings, S. Lazar, F. Swiadek, J. Herrmann, G. J. Norris, C. K. Andersen, M. Müller, A. Blais, C. Eichler, and A. Wallraff, “Realizing repeated quantum error correction in a distance-three surface code,” (2021), arXiv:2112.03708 [quant-ph].

[19] C. Lacroix, P. Mendels, and F. Mila, *Introduction to Frustrated Magnetism: Materials, Experiments, Theory*, Springer Series in Solid-State Sciences (Springer Berlin Heidelberg, 2011).

[20] N. Hatano and M. Suzuki, *Physics Letters A* **163**, 246 (1992).

[21] M. Troyer and U.-J. Wiese, *Phys. Rev. Lett.* **94**, 170201 (2005).

[22] M. Marvian, D. A. Lidar, and I. Hen, *Nature Communications* **10**, 1571 (2019).

[23] M. R. Norman, *Rev. Mod. Phys.* **88**, 041002 (2016).

[24] M. E. Zayed, C. Rüegg, J. Larrea J., A. M. Läuchli, C. Panagopoulos, S. S. Saxena, M. Ellerby, D. F. McMorrow, T. Strässle, S. Klotz, G. Hamel, R. A. Sadykov, V. Pomjakushin, M. Boehm, M. Jiménez-Ruiz, A. Schneidewind, E. Pomjakushina, M. Stingaciu, K. Conder, and H. M. Rønnow, *Nature Physics* **13**, 962 (2017).

[25] Y. Zhou, K. Kanoda, and T.-K. Ng, *Rev. Mod. Phys.* **89**, 025003 (2017).

[26] F. Verstraete and J. I. Cirac, *Physical Review A* **70** (2004), 10.1103/physreva.70.060302.

[27] T.-C. Wei, I. Affleck, and R. Raussendorf, *Physical Review Letters* **106** (2011), 10.1103/physrevlett.106.070501.

[28] A. Miyake, *Annals of Physics* **326**, 1656 (2011).

[29] L. C. Kwek, Z. Wie, and B. Zeng, *International Journal of Modern Physics B* **26**, 1230002 (2012).

[30] A. Kitaev, *Annals of Physics* **303**, 2 (2003).

[31] A. Kitaev, *Annals of Physics* **321**, 2 (2006), arXiv:cond-mat/0506438 [cond-mat.mes-hall].

[32] C. D. Batista and G. Ortiz, *Advances in Physics* **53**, 1 (2004).

[33] L. Isaev, G. Ortiz, and J. Dukelsky, *Journal of Physics: Condensed Matter* **22**, 016006 (2009).

[34] L. Isaev, G. Ortiz, and J. Dukelsky, *Phys. Rev. Lett.* **103**, 177201 (2009).

[35] L. Isaev, G. Ortiz, and J. Dukelsky, *Phys. Rev. B* **79**, 024409 (2009).

[36] D. Huerga, J. Dukelsky, and G. E. Scuseria, *Physical Review Letters* **111** (2013), 10.1103/physrevlett.111.045701.

[37] D. Huerga, J. Dukelsky, N. Laflorencie, and G. Ortiz, *Physical Review B* **89** (2014), 10.1103/physrevb.89.094401.

[38] D. Huerga, S. Capponi, J. Dukelsky, and G. Ortiz, *Phys. Rev. B* **94**, 165124 (2016).

[39] D. Huerga, A. Greco, C. Gazza, and A. Muramatsu, *Phys. Rev. Lett.* **118**, 167202 (2017).

[40] C. Kokail, C. Maier, R. van Bijnen, T. Brydges, M. K. Joshi, P. Jurcevic, C. A. Muschik, P. Silvi, R. Blatt, C. F. Roos, and P. Zoller, *Nature* **569**, 355 (2019).

[41] V. Kuzmin, T. V. Zache, L. Pastori, A. Celi, M. Baranov, and P. Zoller, “Probing infinite many-body quantum systems with finite-size quantum simulators,” (2021), arXiv:2108.12378 [quant-ph].

[42] B. Bauer, D. Wecker, A. J. Millis, M. B. Hastings, and M. Troyer, *Physical Review X* **6** (2016), 10.1103/physrevx.6.031045.

[43] P.-L. Dallaire-Demers and F. K. Wilhelm, *Phys. Rev. A* **93**, 032303 (2016).

[44] Y. Yao, F. Zhang, C.-Z. Wang, K.-M. Ho, and P. P. Orth, *Physical Review Research* **3** (2021), 10.1103/physrevresearch.3.013184.

[45] A. Smith, B. Jobst, A. G. Green, and F. Pollmann, arXiv e-prints , arXiv:1910.05351 (2019), arXiv:1910.05351 [cond-mat.str-el].

[46] M. Foss-Feig, D. Hayes, J. M. Dreiling, C. Figgatt, J. P. Gaebler, S. A. Moses, J. M. Pino, and A. C. Potter, “Holographic quantum algorithms for simulating correlated spin systems,” (2020), arXiv:2005.03023 [quant-ph].

[47] F. Barratt, J. Dborin, M. Bal, V. Stojovic, F. Pollmann, and A. G. Green, *npj Quantum Information* **7** (2021), 10.1038/s41534-021-00420-3.

[48] J.-G. Liu, Y.-H. Zhang, Y. Wan, and L. Wang, *Phys. Rev. Research* **1**, 023025 (2019).

[49] L. Capriotti and S. Sorella, *Phys. Rev. Lett.* **84**, 3173 (2000).

[50] M. Mambrini, A. Läuchli, D. Poilblanc, and F. Mila, *Phys. Rev. B* **74**, 144422 (2006).

[51] S.-S. Gong, W. Zhu, D. N. Sheng, O. I. Motrunich, and M. P. A. Fisher, *Phys. Rev. Lett.* **113**, 027201 (2014).

[52] R. R. P. Singh and R. Narayanan, *Phys. Rev. Lett.* **65**, 1072 (1990).

[53] N. Read and S. Sachdev, *Phys. Rev. Lett.* **66**, 1773 (1991).

[54] H.-C. Jiang, H. Yao, and L. Balents, *Physical Review B* **86** (2012), 10.1103/physrevb.86.024424.

[55] W.-J. Hu, F. Becca, A. Parola, and S. Sorella, *Phys. Rev. B* **88**, 060402 (2013).

[56] L. Wang, D. Poilblanc, Z.-C. Gu, X.-G. Wen, and

F. Verstraete, Physical Review Letters **111** (2013), 10.1103/physrevlett.111.037202.

[57] S. Morita, R. Kaneko, and M. Imada, Journal of the Physical Society of Japan **84**, 024720 (2015), <https://doi.org/10.7566/JPSJ.84.024720>.

[58] L. Wang, Z.-C. Gu, F. Verstraete, and X.-G. Wen, Physical Review B **94** (2016), 10.1103/physrevb.94.075143.

[59] L. Wang and A. W. Sandvik, Physical Review Letters **121** (2018), 10.1103/physrevlett.121.107202.

[60] C. Bravo-Prieto, J. Llumbreras-Zarapico, L. Tagliacozzo, and J. I. Latorre, Quantum **4**, 272 (2020).

[61] A. Kandala, A. Mezzacapo, K. Temme, M. Takita, M. Brink, J. M. Chow, and J. M. Gambetta, Nature **549**, 242 (2017).

[62] D. P. DiVincenzo, D. Bacon, J. Kempe, G. Burkard, and K. B. Whaley, Nature **408**, 339 (2000).

[63] J. Kempe, D. Bacon, D. P. DiVincenzo, and K. B. Whaley, Quantum Inf. Comput. **1**, 33 (2001).

[64] J. Kempe and K. B. Whaley, Phys. Rev. A **65**, 052330 (2002).

[65] R. Jozsa and A. Miyake, Proceedings of the Royal Society A: Mathematical, Physical and Engineering Sciences **464**, 3089 (2008).

[66] D. J. Brod and A. M. Childs, Quantum Information and Computation **14** (2014), 10.26421/qic14.11-12.

[67] D. M. Abrams, N. Didier, B. R. Johnson, M. P. d. Silva, and C. A. Ryan, Nature Electronics **3**, 744 (2020).

[68] Y. Salathé, M. Mondal, M. Oppliger, J. Heinsoo, P. Kurpiers, A. Potočnik, A. Mezzacapo, U. Las Heras, L. Lamata, E. Solano, S. Filipp, and A. Wallraff, Phys. Rev. X **5**, 021027 (2015).

[69] R. Barends, C. M. Quintana, A. G. Petukhov, Y. Chen, D. Kafri, K. Kechedzhi, R. Collins, O. Naaman, S. Boixo, F. Arute, K. Arya, D. Buell, B. Burkett, Z. Chen, B. Chiaro, A. Dunsworth, B. Foxen, A. Fowler, C. Gidney, M. Giustina, R. Graff, T. Huang, E. Jeffrey, J. Kelly, P. V. Klimov, F. Kostritsa, D. Landhuis, E. Lucero, M. McEwen, A. Megrant, X. Mi, J. Mutus, M. Neeley, C. Neill, E. Ostby, P. Roushan, D. Sank, K. J. Satzinger, A. Vainsencher, T. White, J. Yao, P. Yeh, A. Zalcman, H. Neven, V. N. Smelyanskiy, and J. M. Martinis, Phys. Rev. Lett. **123**, 210501 (2019).

[70] B. Foxen, C. Neill, A. Dunsworth, P. Roushan, B. Chiaro, A. Megrant, J. Kelly, Z. Chen, K. Satzinger, R. Barends, F. Arute, K. Arya, R. Babbush, D. Bacon, J. C. Bardin, S. Boixo, D. Buell, B. Burkett, Y. Chen, R. Collins, E. Farhi, A. Fowler, C. Gidney, M. Giustina, R. Graff, M. Harrigan, T. Huang, S. V. Isakov, E. Jeffrey, Z. Jiang, D. Kafri, K. Kechedzhi, P. Klimov, A. Krotkov, F. Kostritsa, D. Landhuis, E. Lucero, J. McClean, M. McEwen, X. Mi, M. Mohseni, J. Y. Mutus, O. Naaman, M. Neeley, M. Niu, A. Petukhov, C. Quintana, N. Rubin, D. Sank, V. Smelyanskiy, A. Vainsencher, T. C. White, Z. Yao, P. Yeh, A. Zalcman, H. Neven, and J. M. Martinis (Google AI Quantum), Phys. Rev. Lett. **125**, 120504 (2020).

[71] N. Lacroix, C. Hellings, C. K. Andersen, A. Di Paolo, A. Remm, S. Lazar, S. Krinner, G. J. Norris, M. Gabureac, J. Heinsoo, A. Blais, C. Eichler, and A. Wallraff, PRX Quantum **1**, 110304 (2020).

[72] D. González-Cuadra, (2021), arXiv:2107.10122 [cond-mat.quant-gas].

[73] R. H. Byrd, P. Lu, J. Nocedal, and C. Zhu, SIAM Journal on Scientific Computing **16**, 1190 (1995), <https://doi.org/10.1137/0916069>.

[74] C. Zhu, R. H. Byrd, P. Lu, and J. Nocedal, ACM Trans. Math. Softw. **23**, 550 (1997).

[75] H. Araki, T. Mizoguchi, and Y. Hatsugai, Phys. Rev. Research **2**, 012009 (2020).

[76] Y. You, J. Bibo, and F. Pollmann, Phys. Rev. Research **2**, 033192 (2020).

[77] C. Monroe, W. Campbell, L.-M. Duan, Z.-X. Gong, A. Gorshkov, P. Hess, R. Islam, K. Kim, N. Linke, G. Pagano, and et al., Reviews of Modern Physics **93** (2021), 10.1103/revmodphys.93.025001.

[78] J. Schulenburg, A. Honecker, J. Schnack, J. Richter, and H.-J. Schmidt, Phys. Rev. Lett. **88**, 167207 (2002).

[79] R. Sagastizabal, X. Bonet-Monroig, M. Singh, M. A. Rol, C. C. Bultink, X. Fu, C. H. Price, V. P. Ostroukh, N. Muthusubramanian, A. Bruno, and et al., Physical Review A **100** (2019), 10.1103/physreva.100.010302.

[80] F. Kobayashi, K. Mitarai, and K. Fujii, “Parent hamiltonian as a benchmark problem for variational quantum eigensolvers,” (2021), arXiv:2109.11759 [quant-ph].